Field data examples

Efficient and accurate prestack depth migration plays an important role in both the imaging and velocity analysis of seismic reflection data collected in areas of lateral velocity variation. If such an imaging method is implemented using a Kirchhoff integral approach, the largest part of the effort in migrating data is the computation of the traveltimes and geometrical amplitudes of seismic waves in a given interval velocity model. Chapters **??** and **??** present two wavefront-propagation methods for rapid calculation of the traveltimes and geometrical amplitudes in a general 2-D velocity model. With these two methods, the computational cost of Kirchhoff depth migration is considerably reduced. Chapter **??** presents a residual depth migration algorithm that converts an image migrated with one velocity model to an image migrated with another velocity model. This algorithm further reduces the computational cost of depth migration when data are to be migrated with successive velocity models, as in prestack depth migration velocity analysis.

This chapter describes an application of these methods to a field dataset. I first describe the dataset and its preprocessing. I then show how the interval velocity model is estimated through an iterative procedure of prestack depth migration and velocity analysis. After that, I illustrate the residual depth migration by comparing its result with the image obtained with full depth migration, which leads to the conclusions.

Data description and preprocessing

The field dataset is part of a marine survey collected offshore in southern California. The recording cable has 36 channels with a near offset of 65.71 m and a uniform group interval of 33.33 m, which yields a maximum offset of 1.22 km. The shot interval is 8.33 m. Clearly, the survey has a smaller maximum offset and finer spatial sampling than usual. The signals are recorded with 2 ms time-sampling intervals and have a wide frequency band ranging from 10 Hz to 100 Hz. I sorted the data into constant offset sections. Figure 1 shows a near offset section and a far offset section. The complex subsurface structure generates many diffracted events. These events cross one another and make it difficult to interpret the raw data before migration. Strong water-bottom multiples also appear in the sections. However, because the depth variation of the sea floor is smooth, the multiples are clearly distinguishable from other useful events. In the migration process, I ignored the presence of these multiples. They would be attenuated when images migrated from different constant offset sections were stacked. Figure 2 shows two common-midpoint (CMP) gathers.

Most events are well approximated by hyperbolic moveout, partly because most parts of the medium have smooth lateral velocity variations and partly because the data have a small maximum offset. However, a few non-hyperbolic events can still be identified, which suggests the application of prestack depth migration.

The dataset is from the same survey line used as an illustration in Fowler (1988) and Sword (1987). Fowler used this dataset to demonstrate his time-migration velocity analysis. He noted that the energy source for the survey was a pair of water guns, with a weak first pulse followed by a second strong, sharp pulse. Because the zero timing is measured from the firing of the first water gun, the time delay between the two pulses causes systematic bias in the velocity analysis. Sword solved this problem by applying a static time shift to the data. The amount of time shift is estimated by calibrating the result of velocity analysis with the water velocity, which is known to be 1.48 km/s. I have used a simple deconvolution algorithm to remove the timing errors caused by the double-pulse wavelet.

Dephasing filter

The traveltimes of seismic waves in a given medium can be computed efficiently by using the wavefront propagation methods described in Chapters **??** and **??**. These traveltimes predict the arrival times of events on seismic sections. If the data are to be imaged using Kirchhoff migration, it is desirable that the predicted arrival time of an event coincide with the peak of the wavelet of the event. Because the wavelets of events are usually well approximated by the source wavelet, the goal can be achieved by applying to the data a filter of the following form (Claerbout, 1991):

$$F(\omega) = \frac{W^*(\omega)}{|W(\omega)|^\alpha + \lambda\sigma_W^\alpha}, \tag{1}$$

where $*$ stands for the complex conjugate, $W(\omega)$ and σ_W^2 are the spectrum and average power of the source wavelet, respectively, and α and λ are constants with $0 \leq \alpha \leq 2$ and $0 \leq \lambda \leq 1$, respectively. Because the field dataset has a wide frequency band, I choose to have an allpass filter by setting $\alpha = 1$ and $\lambda = 0$ so that the filter would not change the amplitude spectrum of input data, but would remove the phase of the wavelet of input data. For this reason, I call it dephasing filter.

I have estimated the source wavelet of the field data from the water-bottom reflection. The result is shown in Figure 3. The double pulses are clearly visible. I then applied the dephasing filter to the data. Figure 4 compares the sample traces before and after dephasing. After dephasing, the wavelets of events become approximately zero-phase. The traces are effectively shifted backward in time by a static shift of approximately 50 ms, which agrees more or less with Sword's estimate (Sword, 1987). Events after dephasing are easier to identify than before, whereas the amplitude spectrum is unchanged.

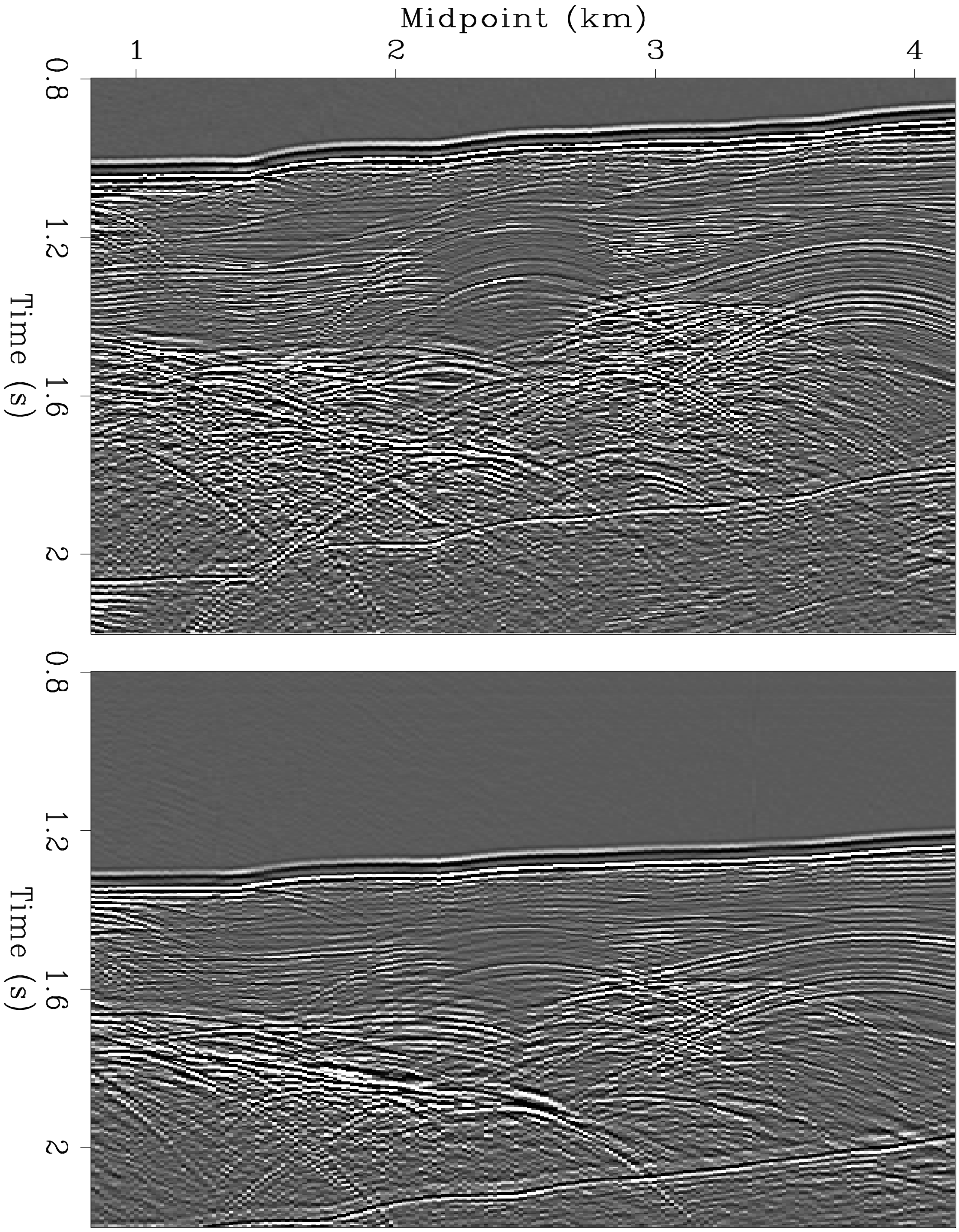

Figure 1: Constant offset sections. Top: a near offset section with an offset of 65.71 m. Bottom: a far offset section with an offset of 1.22 km. Many diffracted events are clearly identifiable in both sections. fiedat5-fienf [ER]

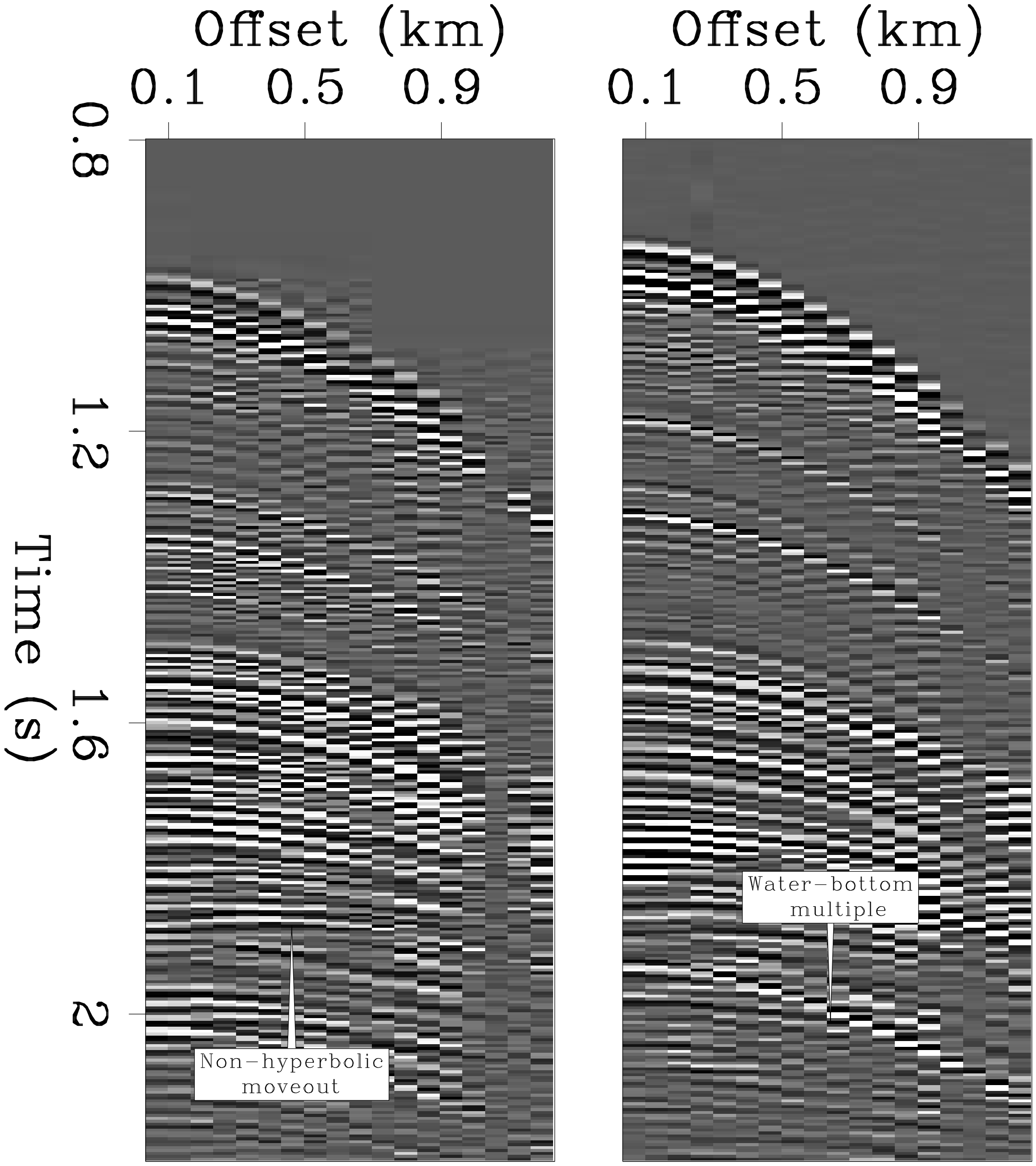

Figure 2: Common midpoint gathers. Left: at midpoint 1.53 km. Right: at midpoint 2.56 km. Although most events have approximately hyperbolic moveout, a few non-hyperbolic events can be identified. Strong water-bottom multiples can also be identified. fiedat5-fiecmp [ER]

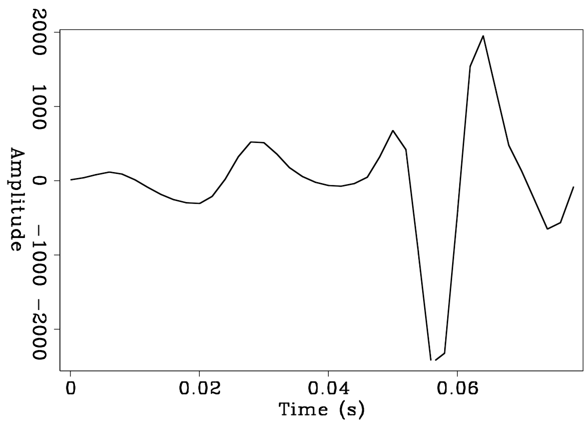

Figure 3: The source wavelet estimated from the water-bottom reflection. fiedat5-fiewlt [ER]

Determination of the interval velocity model

Depth migration of seismic reflection data requires the accurate knowledge of the interval velocity field in the area where the dataset was collected. Interval velocities can be estimated from prestack seismic reflection data. Prestack depth migration of constant offset sections produces an image cube. Two axes of this cube are the horizontal and depth coordinates of images, and the third axis indicates the offsets. Slicing the image cube by a plane perpendicular to the offset axis gives the image migrated from a constant offset section. Slicing it by a plane perpendicular to the axis indicating the horizontal coordinates gives the image of the subsurface at a common surface location, which is often referred to as a common-surface-location (CSL) gather.

If an estimated velocity model correctly models the propagation of seismic events recorded with different source-receiver offsets, depth images migrated from different constant offset sections resemble one another. Therefore, the subsurface images in each CSL gather are horizontally coherent. However, if an incorrect velocity model is used in depth migration, CSL gathers do not always display horizontally coherent images. Figure 5 shows the result of prestack depth migration of the field dataset with a laterally invariant velocity model. The top panel shows the stacked image after prestack depth migration. The bottom part of the figure displays eight CSL gathers. Clearly, the images in these gathers are not always horizontally coherent. Some of them have positive residual moveout (curve downwards), whereas others have negative residual moveout (curve upwards). Thus, direct stacking of these images does not coherently enhance the final image.

The moveout of images in CSL gathers indicates the existence of errors in the estimated interval velocity model, and can thus be used to estimate the velocity perturbations that tend to produce more horizontally coherent images. Several existing methods of prestack depth migration velocity analysis are based on this principle (Deregowski, 1990; van Trier, 1990; Etgen, 1990). In these methods, the velocity perturbations are estimated through an optimization process. New images are subsequently obtained by migrating data with the updated velocity model. The process of migration and velocity estimation is repeated until the perturbations of interval ve-

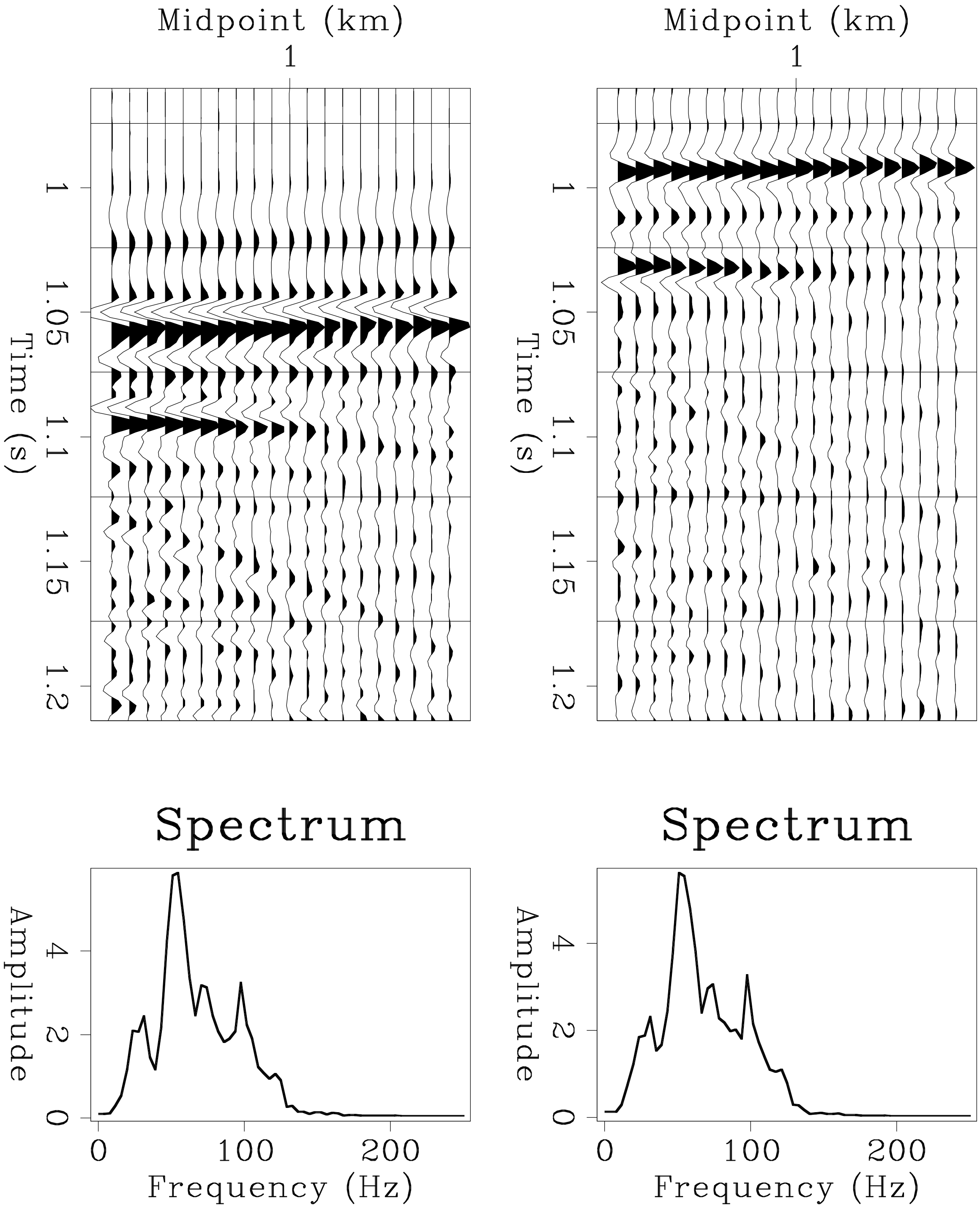

Figure 4: Comparison of sample traces before (left) and after (right) dephasing. Two bottom panels show the amplitude spectra. fiedat5-fiecom [ER]

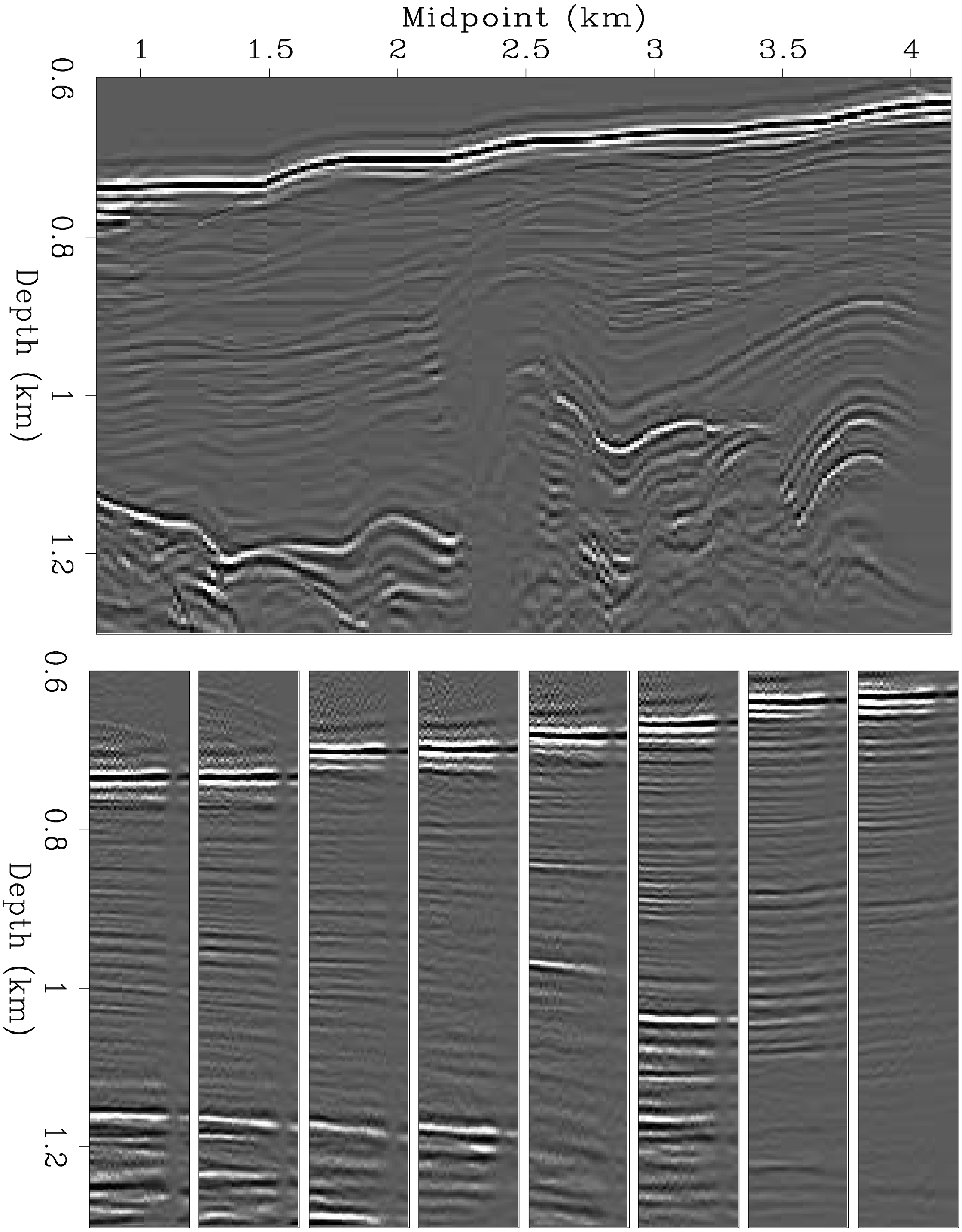

Figure 5: The result of prestack depth migration with a laterally invariant velocity model. Top: the stacked image of depth-migrated constant offset sections. Bottom: eight common surface location gathers. The images in the first five gathers have positive residual moveout and the images in the last two gathers have negative residual moveout. fiedat5-fieimgavg [ER]

locities no longer improve the offset coherence of the images. I have generally followed this iterative approach to estimate the interval velocity model for the field dataset. I used Kirchhoff prestack depth migration to obtain the images from different common offset sections, and estimated interval velocities by manual picking and adjustment. The seismic traveltimes and geometrical amplitudes needed for Kirchhoff depth migration are efficiently computed by the wavefront propagation methods presented in Chapters **??** and **??**.

Using Kirchhoff depth migration, one can compute the image samples at individual subsurface points. To reduce the cost of prestack depth migration, I migrated the field dataset to obtain a sparsely sampled image cube. The images in the cube can be spatially aliased along all three axes, for which automatic scanning and picking used in the migration velocity analysis may not work well. However, spatial aliasing becomes less of a problem if the velocity estimation is done through manual picking and adjustment. Manual operation also allows one to identify multiple reflections, out-plane reflections, and other coherent noises, on the basis of personal experience. The major disadvantage of manual operation is its inaccuracy in estimating interval velocities.

The parameterization of a velocity model has an important impact on the process of interval velocity estimation. Whereas unnecessary parameters increase the computational cost, an insufficient number of parameters leads to a poor approximation to the true model. Because it is known that the area where the field data were collected has a smoothly varying velocity field, I used a piecewise-linear function to approximate the true interval velocity model. To construct such a velocity field, I manually pick major reflectors on an initially depth-migrated image and specify the interval velocities at sparsely sampled points along the picked reflectors. The picked reflectors divide the velocity model into layers. The sampled interval velocities are first interpolated linearly along the picked reflectors, and subsequently interpolated linearly in depth within each layer.

Instead of estimating all the sparsely sampled interval velocities simultaneously, I have adopted a layer-to-layer approach. I first filled the water layer with a constant velocity of 1.48 km/s so that after migration the images of the sea floor were horizontally coherent in all CSL gathers. Next, I adjusted the interval velocities that were sparsely sampled along the picked reflector next to the sea floor, until the migrated images of all the reflectors within the layer between the sea floor and the picked reflector had zero residual moveout. I fixed the estimated interval velocities within this layer and moved to the next layer. The above procedure was repeated for all the layers. It should be noted that the adjustment of interval velocities changes the image positions of reflectors. Therefore, in principle, a reflector should be repicked when the sampled interval velocities above the reflector are adjusted. However, because I used a smooth velocity representation, repicking reflectors is actually necessary only when large velocity adjustments were made. Figure 6 displays the final result of the velocity estimation. The top panel of the figure shows the positions of six major reflectors that were picked manually, and the bottom panel shows the estimated interval velocity field. The spatial variations of velocity are extensive although the magnitudes of the variations are relatively small.

I have migrated the field data with the estimated interval velocity field. The result is shown in Figure 7. The top panel of the figure displays the stacked image of depth-migrated constant offset sections. Steep dipping reflectors are well imaged. The terminations of reflectors at the locations of several faults are well defined. Compared with the stacked image in Figure 5, the new image has better resolution, especially around the surface location of 2.5 km and depth of 0.95 km. The bottom part of this figure displays eight CSL gathers whose surface locations match the gathers shown in Figure 5. It can be seen that the images in these gathers have approximately zero residual moveout, which proves the accurate estimation of interval velocity field. The only exception appears at the depth of 1.2 km and in the fifth gather from the left. Correcting the residual moveout of this image would require an extremely low velocity overburden. Therefore, I believe that this image results from out-plane reflection or migration artifact.

Residual depth migration

I have used the zero offset section of the field data and the interval velocity model shown in Figure 6 to illustrate the residual depth migration described in Chapter **??**. I first migrated the zero offset section with a constant velocity of 1.48 km/s. The image obtained is displayed in the top panel of Figure 8. Clearly, the images of reflectors below the sea floor are under-migrated and mispositioned. I then applied the residual depth migration to this initially migrated image and obtained an image shown in the bottom panel of Figure 8. I expected that the residual depth migration can convert the image migrated with the constant velocity into the image migrated with the estimated interval velocity field shown in Figure 6. Figure 9 compares the image after residual depth migration and the image migrated directly with the estimated interval velocity field. As expected, the two images closely resemble each other, but the cost of residual depth migration is about one quarter of the cost of the full depth migration. This example shows a successful application of residual depth migration to the field data.

Conclusions

I have successfully applied the methods presented in this thesis to the field data. I used the wavefront propagation methods to calculate the traveltimes and geometrical amplitudes so that the prestack depth migration in each iteration of the depth-migration velocity analysis can efficiently be accomplished. Migration with the estimated interval velocity model improves the stacked image. I also demonstrate the residual depth migration on the zero-offset section of the field data, which proves that the residual depth migration can correct the positional distortion of the images migrated initially with a wrong velocity model.

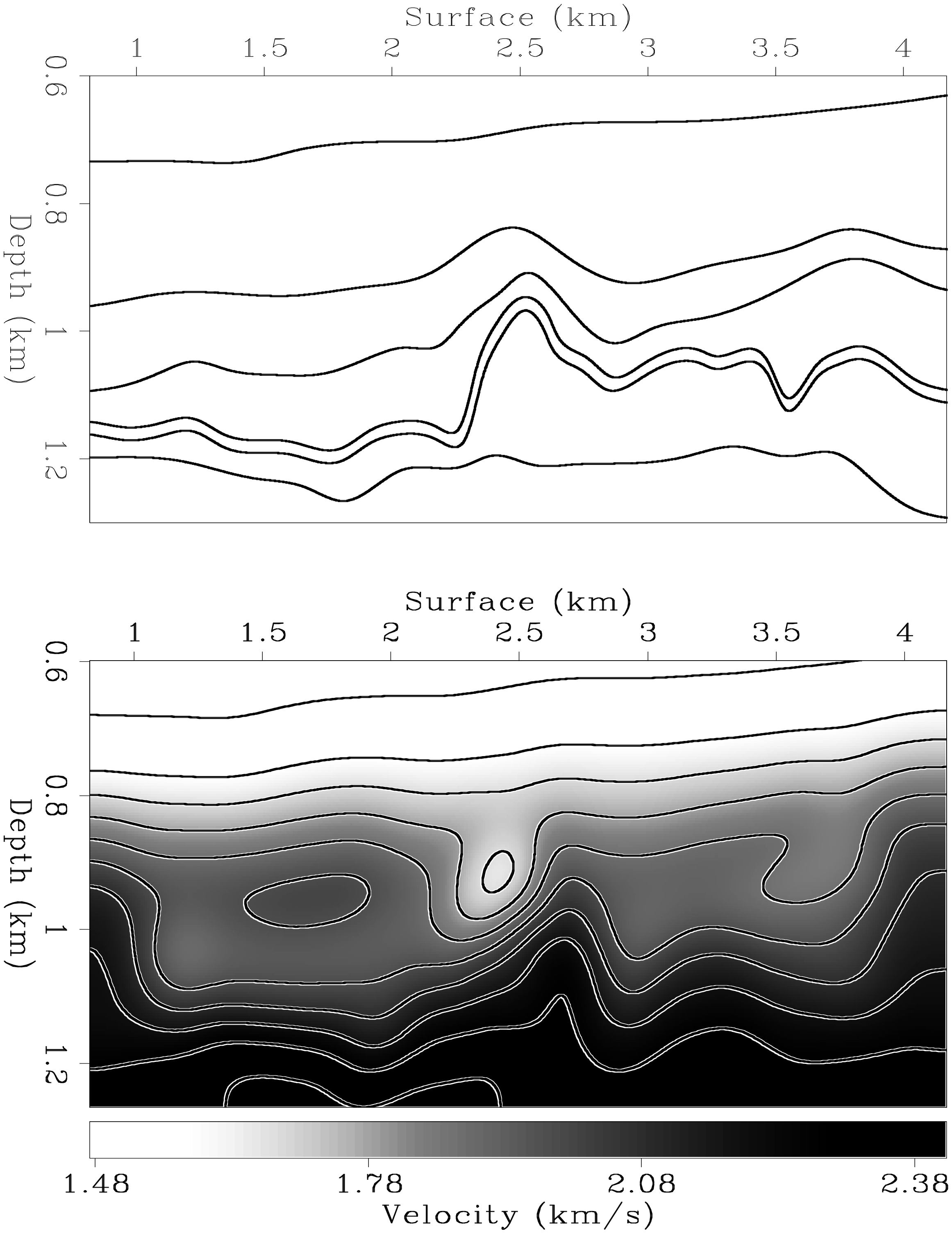

Figure 6: The final result of the velocity estimation. Top: the positions of six manually picked reflectors. Bottom: the estimated interval velocity field. The contour intervals are 0.1 km/s. fiedat5-fievel [ER]

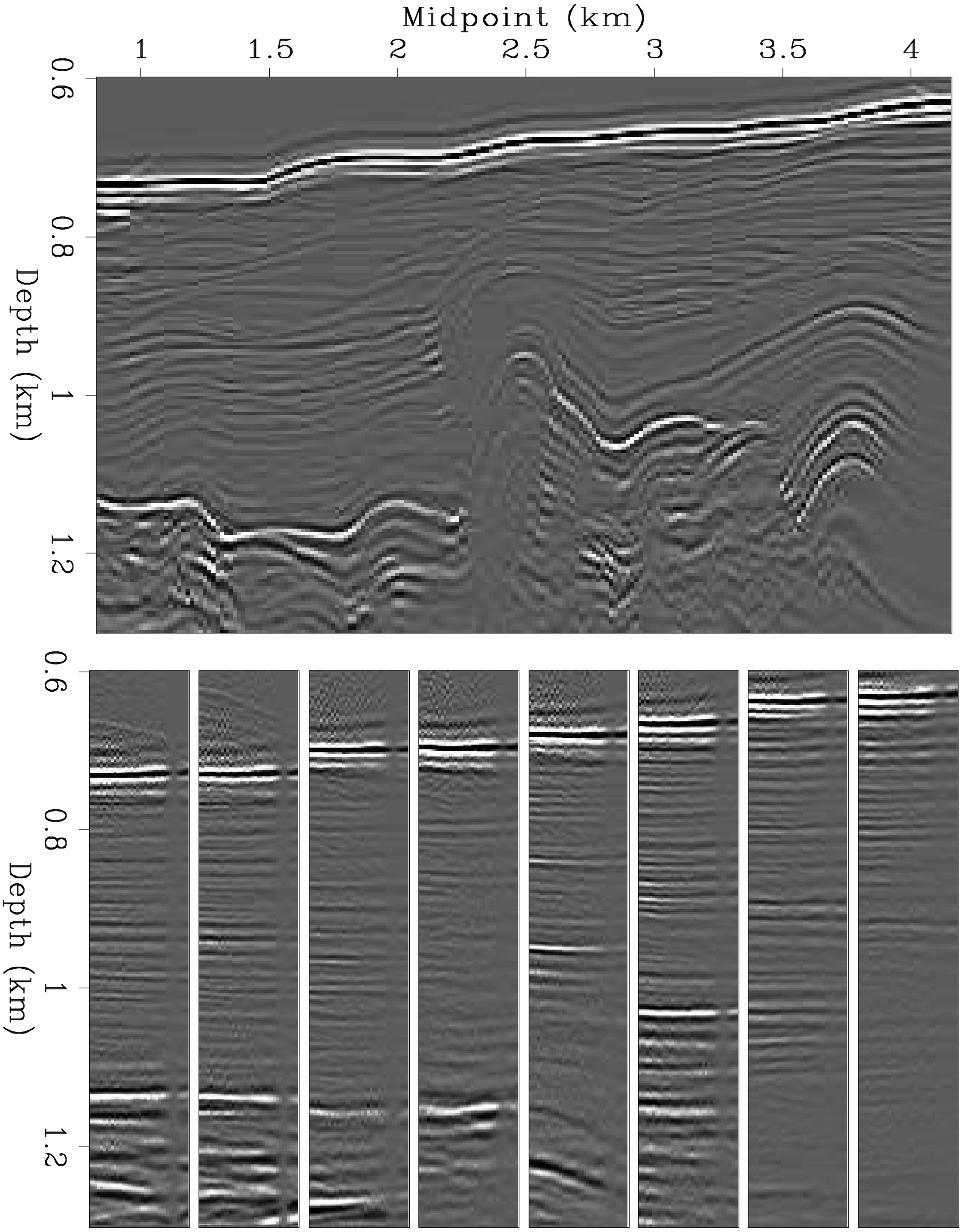

Figure 7: The result of prestack depth migration with the estimated velocity model. Top: the stacked image of depth-migrated constant offset sections. Bottom: eight common surface location gathers. fiedat5-fieimg [ER]

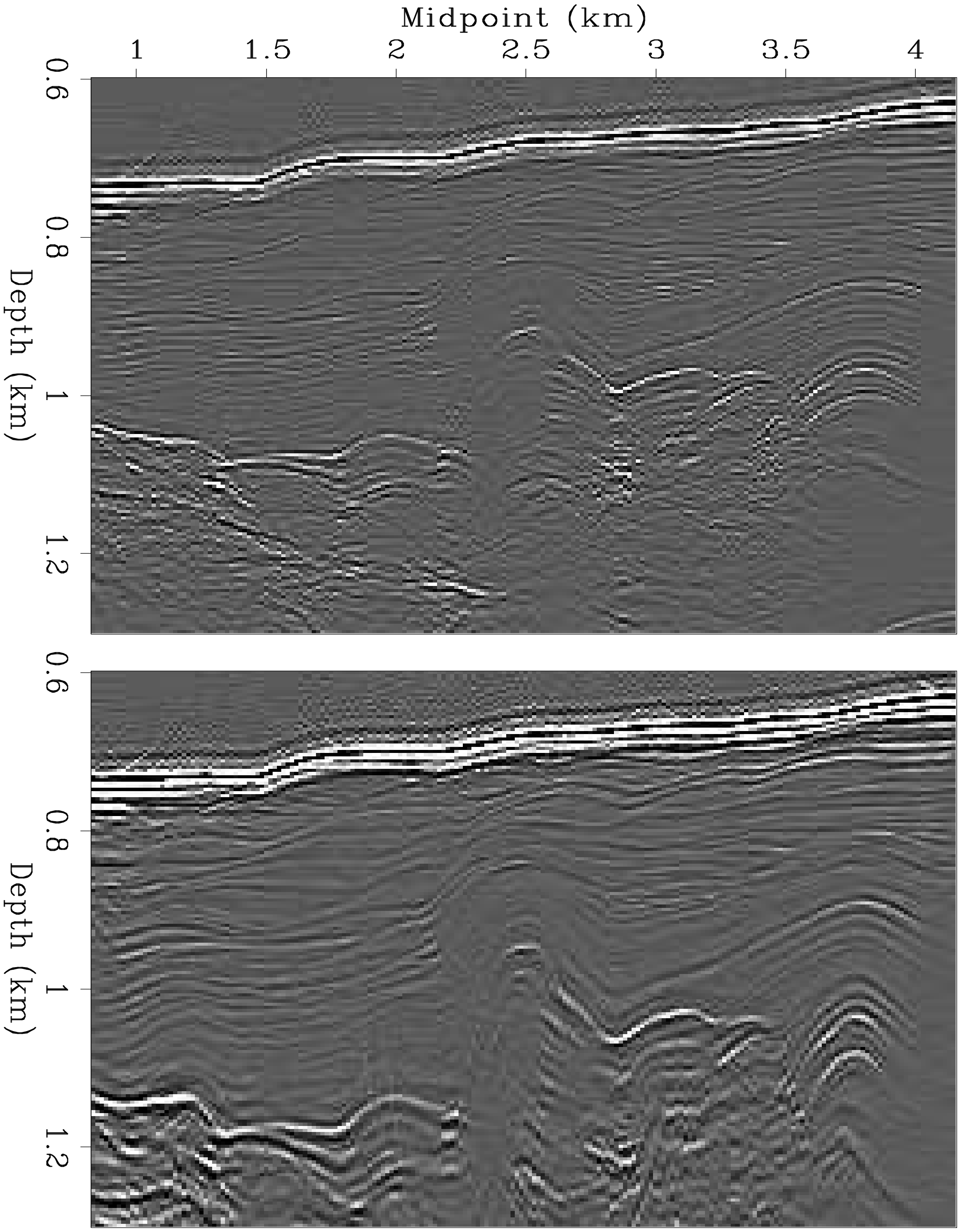

Figure 8: Top: the image migrated with a constant velocity of 1.48 km/s. Bottom: the image after residual depth migration. fiedat5-fieimgv0 [ER]

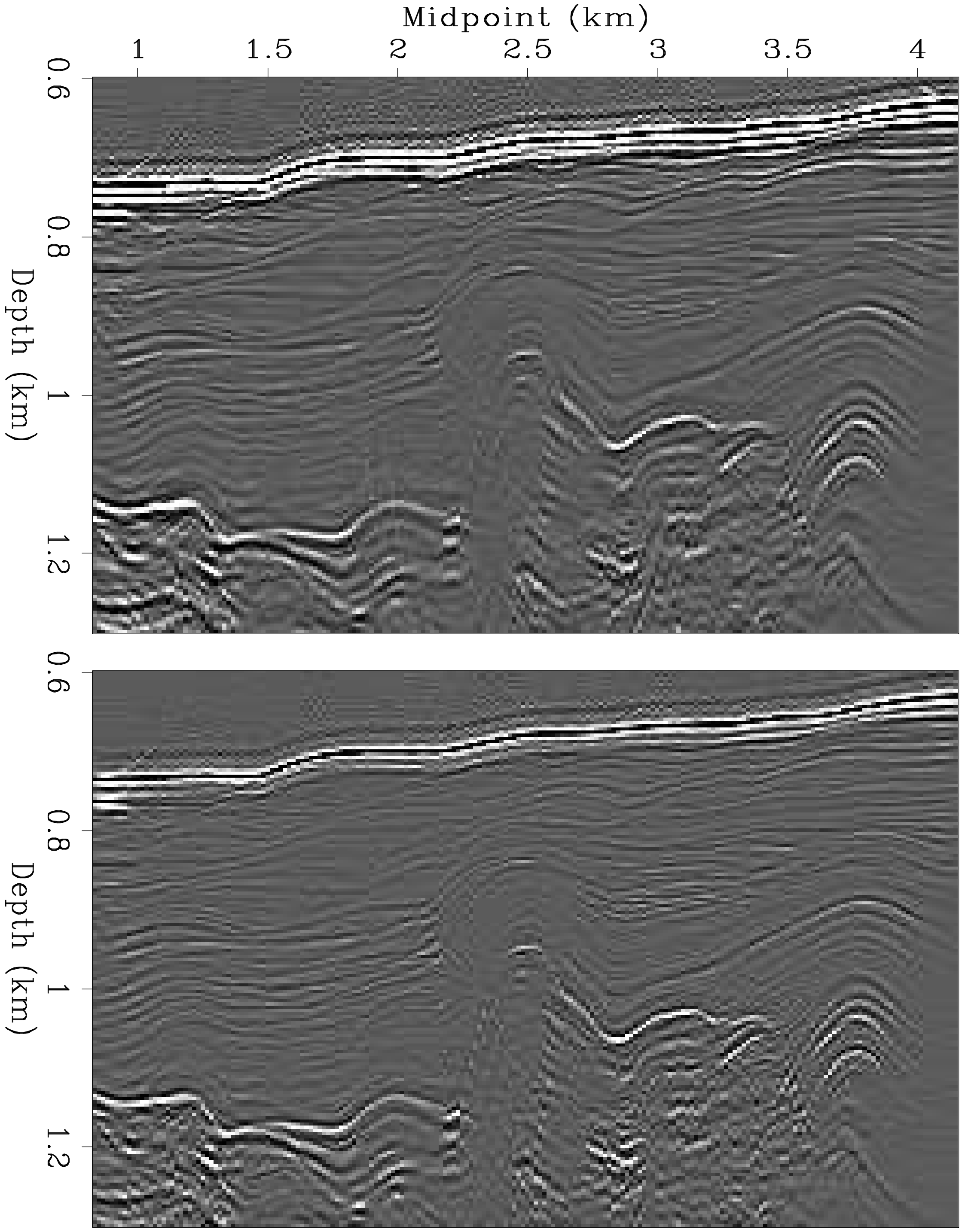

Figure 9: Comparison of residual depth migration and full depth migration. Top: the image obtained by residual depth migration. Bottom: the image obtained by full depth migration. fiedat5-fiermg [ER]